Surfaces and Interfaces 90 (2026) 109259

Contents lists available at ScienceDirect

Surfaces and Interfaces

journal homepage: www.sciencedirect.com/journal/surfaces-and-interfaces

Electron beam ion-assisted deposition of SiO_2–TiO_2 broadband antireflection coatings: Substrate temperature effect on optical properties

Omprakash Muthusamy [a,*], Yasir Joya [b], Richard Day [a], Chris Nyamayaro [a], Ben Assinder [c], Sohail Khan [c], Matthew Jevon [d], Zengbo Wang [c]

[a] Wrexham University, St Asaph Business Park, St Asaph LL17 0JD, UK
[b] Glyndwr Innovations Ltd, OpTIC Technology Centre, St Asaph Business Park, Ffordd William Morgan, St Asaph, LL17 0JD, UK
[c] School of Computer Science and Engineering, Bangor University, Dean Street, Bangor, Gwynedd LL57 1UT, UK
[d] Physics Department, Aberystwyth University, Penglais, Aberystwyth, Ceredigion SY23 3BZ, UK

ARTICLE INFO

Keywords:
SiO_2-TiO_2 multilayers
E-beam ion-assisted deposition
Anti-reflection coating
Raman spectroscopy
Film stability
Porosity

ABSTRACT

Antireflection coatings dominate a critical role in enhancing optical efficiency across a wide range of technologies, particularly top layer in high-performance solar energy systems and advanced laser optics. In this study we report fabricating low-loss SiO_2–TiO_2 based antireflection coating by using electron beam ion-assisted deposition and analysing their optical transmission evolved through microstructural transformation under a varying thermal load. Multilayer antireflection films were deposited on cleaned glass substrates at temperature range from 120°C to 240°C, with precise control over layer thickness *in-situ*. Optical spectral analysis revealed average transmission values of 99.54 ± 0.04 % in the 470–532 nm range and 98.63 ± 0.12 % in the 950–1064 nm range at substrate temperature of 160°C and 180°C, representing significant improvement over uncoated glass. The spectral transmission of AR coatings dropped beyond this temperature owing to increased roughness, porosity, and microstructural transformation resulting in a decreased optical efficiency. Adhesion and aging tests confirmed excellent interfacial stability and durability. Water contact angle analysis indicated the hydrophilic nature of the film surface. These findings showcase the effectiveness of electron beam ion-assisted deposition process in fabricating high-precision industrial quality antireflection coating by *in-situ* optimization of substrate temperature.

1. Introduction

Antireflection (AR) coatings are crucial for improving optical transmission across various applications, including solar panels, ophthalmic devices, display systems, aerospace and defence optics, and high-power laser components [1]. Typically, AR coating employs alternating layers of materials with high and low refractive indices to induce destructive interference and minimize surface reflection [2]. However, single-layer coatings are limited to narrow spectral ranges due to the wavelength-dependent nature of the quarter-wavelength interference condition, which limits the applicability in broadband applications [3].

To achieve zero reflectance, the refractive index and thickness of the film must satisfy the following conditions [4,5]:

Refractive index:

$$n_1 = \sqrt{n_0 n_s} \tag{1}$$

Thickness:

$$d = \frac{\lambda}{4n_1} \tag{2}$$

Where n_1, n_0, n_s, λ represents the refractive index of the film, air, substrate, and reference wavelength, respectively.

For broadband applications, multilayer AR structures, where alternating stack of high and low-index materials are commonly employed to achieve superior performance [6]. Various dielectric materials such as Al_2O_3 [7], HfO_2 [8], MgF_2 [9], TiO_2 [10], SiO_2 [11] have been investigated for these purposes. Among these, TiO_2 and SiO_2 are particularly advantageous due to their complementary refractive indices TiO_2 (2.1–2.45) [12–14] and SiO_2 (1.46–1.47) [15,16] and their high transparency from the visible to near-infrared (NIR) range. In addition, both materials are non-toxic, earth-abundant, chemically and thermally stable, and low cost [17–21].

* Corresponding author.
E-mail address: omprakash.muthusamy@wrexham.ac.uk (O. Muthusamy).

https://doi.org/10.1016/j.surfin.2026.109259
Received 30 August 2025; Received in revised form 6 March 2026; Accepted 10 April 2026
Available online 11 April 2026

Multilayer SiO_2-TiO_2 AR coating have been fabricated using various deposition techniques such as sol-gel, which provides compositionally tuneable coating, but typically surfers from high porosity, undesirable interfacial reaction due to high temperature annealing, weak adhesion, and poor environmental stability [22,23], plasma enhanced chemical vapor deposition (PECVD) enables better film densification and composition control at relatively low substrate temperature, however, precursor, processing gas, and by products are toxic to the environment [24]. Spray pyrolysis offers simple, scalable route for the large area coatings; however, chemical homogeneity reduced due to residue organics remaining in the processed coatings [25].

On the other hand, physical vapor deposition such as magnetron sputtering [26,27], Ion beam sputtering (IBS) [28,29], and electron beam deposition (EBD) have been widely used [30,31]. Magnetron sputtering and IBS produce dense, low-loss multilayers with excellent uniformity and durability. However, these methods rely on sophisticated vacuum system and process control resulting in low deposition rate and high running cost restricting the use of niche market. EBD is an attractive technique, based on thermal evaporation process, offers higher deposition rate and low cost in producing high quality multi-component AR coatings suited to industrial applications. However, there are challenges in developing defect-free multilayer coating by EBD with high optical transmission due to columnar microstructure growth of TiO_2 leading to poor adhesion and environmental stability, which require additional metal coating to improve interfacial adhesion [32,33]. Electron beam ion-assisted deposition (EB-IAD) is one of the leading thin-film creating techniques that addresses these challenges by incorporating ion-bombardment during deposition resulting in improving film density, chemical and microstructural uniformity, precise coating thickness, improved bonding and interfacial adhesion, high reproducibility and superior durability, high laser damage threshold, making EB-IAD one of the most sustainable technology for industrial laser optics [34,35].

Notably, optical properties of TiO_2 thin film are strongly influenced by substrate temperature and post-deposition thermal annealing due to changes in microstructure. For example, Yang et al. reported that TiO_2 films deposited at 300°C and annealed at 450°C for 1 h exhibited a 28 % higher transmission in the 400–800 nm range than films deposited at 150°C, attributed to improved structural uniformity and reduced defects [36]. Conversely, Obstarczyk et al. observed an 8 % decrease in visible transmission after annealing at 800°C, resulting from the formation of a bi-layer microstructure in EB-IAD-deposited TiO_2 films [37]. These findings highlight that thermal annealing can either enhance or degrade optical performance depending on its impact on microstructure and crystallinity. Rao et al. fabricated SiO_2 film by EBD with assistance of ionised oxygen and found only minor changes in optical properties with substrate temperature and post thermal annealing [38].

Unlike most previous studies that primarily focus on achieving high transmission and improved quality of AR coatings through post-thermal annealing or surface functionalization, such post processing treatment can deteriorate the optical performance due to change in thickness, refractive index, and structural modification. This work aims to elucidate how *in-situ* substrate temperature regulates surface microstructure and interfacial integrity during electron-beam-ion assisted deposition (EB-IAD) to achieve higher optical transmission over a broad range of 460 – 1100 nm (including key laser wavelengths at 532 nm and 1064 nm) without post processing treatments. By correlating temperature-dependent growth conditions with microstructure, structural phase analysis, environmental stability, and broad optical response, a clear structure-property relationship is established. The results identify an optimal *in-situ* processing window that promotes dense and smooth surface morphology, leading to durable, high-transmission broadband AR coating. This study provides practical insights for laser and solar energy system.

2. Experimental procedure

High-purity SiO_2 (99.99 %) and Ti_3O_5 (99.99 %) granules were used for deposition on double-side polished D263 glass substrates (25 mm diameter, 1 mm thickness). Prior to deposition, the substrates were ultrasonically cleaned in isopropyl alcohol and acetone, followed by drying using an ionized air gun. The deposition was performed using a SYRUSpro 1350 system equipped with dual electron beam guns (EBG1 for SiO_2, EBG2 for TiO_2), an ion source, a neutralizer, and a rotating Calotte holder. High vacuum generated with a diffusion pump and base pressure was maintained at 5×10^{-6} mbar. IAD was performed at 6500 W combined with Ar + O_2 flow of 120 sccm. The neutralizer was employed to mitigate potential film damage from ion bombardment. The substrate was rotated at 50 rpm to ensured uniform coating thickness. Deposition rates were continuously monitored using a quartz crystal microbalance system (QCMS), with rates set at 0.4 nm/s for SiO_2 and 0.3 nm/s for TiO_2. A Meissner trap, maintained at −150°C, was used to capture residual water vapor and accelerate the pump-down process.

Film thickness calibration was conducted prior to multilayer deposition, using separate depositions of 270 nm TiO_2 on D263 glass (n = 1.52) and 275.6 nm SiO_2 on high-index glass (n = 1.8, O'Hara T1H6). The thicknesses were verified by comparing the measured and simulated transmission spectra. An eight-layer AR coating with structure air/$(HL)^4$/substrate was designed using Mcalc software (developed by Bühler) for the 300–1100 nm wavelength range, where H and L denote TiO_2 and SiO_2, respectively. AR coating design was carried out by following characteristic matrix method, as described in the supplementary information. The individual layer thicknesses were optimized using the needle optimization function, and the thickness values are listed in Table 1. The multilayer films were deposited at substrate temperatures of 120°C, 160°C, 180°C, 200°C, and 240°C to investigate the temperature dependent microstructure and phase evolution of EB-IAD multilayer AR coating. After full deposition cycle, substrates were cooled to room temperature under vacuum to preserve film stoichiometry from post-deposition oxidation and prevent moisture uptake. This controlled temperature sequence enables a comprehensive understanding of how substrate temperature contributes to film morphology and optical response. The experiment was performed in triplicate for each temperature to analyse AR coatings reproducibility. The error bars were calculated using standard mean error (SME) in Eq. (3).

$$SME = \frac{\sigma}{\sqrt{N}} \tag{3}$$

Where, N is the number of replicates, σ is the standard deviation

Optical transmission and reflection spectra were measured across the 400–1100 nm range using an Agilent Cary 7000 Universal Measurement Spectrophotometer (UMS) with scan rate of 600 nm/min. The data was collected at each 1 nm interval. Surface morphology and roughness were characterized using tapping-mode atomic force microscopy (AFM, Veeco Dimension 3100/V) over a 5 μm × 5 μm area. The AFM measurements were performed using a silicon probe with a nominal tip radius of approximately < 10 nm. The average surface (R_a) roughness and average root mean square (RMS) roughness (R_q) were determined

Table 1
Designed thickness of multilayer broadband AR coating.

Number of layers	Material	Thickness (nm)	Refractive index
1	SiO_2	114.02	1.46
2	TiO_2	30.38	2.41
3	SiO_2	19.96	1.46
4	TiO_2	83.53	2.41
5	SiO_2	18.67	1.46
6	TiO_2	35.83	2.41
7	SiO_2	48.39	1.46
8	TiO_2	12.32	2.41
	Substrate		1.52

from six randomly selected regions within each AFM image using Gwyddion software (2.67) and their corresponding grain size was estimated using texture *(line-profile)* function. The texture function extracts a height profile along a selected scan line, and the lateral dimensions of surface features were estimated from the peak-to-peak distances along the *x*-axis of the profile.

Film adhesion was assessed in accordance with ISO 9211–4 by firmly applying 3 M scotch tape to the deposited film and removing it at a 180° angle. The film was then visually inspected under reflected light for any sign of coating removal, and transmission spectra were recorded before and after the tape test to verify the optical performance. In addition, a cross-hatch tape test was performed following ASTM D3359. A lattice pattern cut was made on the film using stainless steel blade with 1 mm spacing. A tape was then attached firmly over the grid, ensuring no air trapped beneath it, and subsequently removed at a 180° angle. After tape removal, the substrate was examined using an optical microscope (Nikon ECLIPSE E600) in bright field mode to detect any peeling or delamination of coating. Adhesion strength was evaluated using the ASTM D3359 rating method. The aging behaviour was evaluated by maintaining the sample at ambient conditions for 60 days and re-measuring their optical spectra.

The water contact angle measurements were performed to assess the wettability of the SiO_2–TiO_2 multilayer coatings as a function of substrate temperature. These properties are directly linked to nanoscale roughness and porosity, which also influence environmental stability and long-term optical performance. Water contact angles were measured using Ossila L2004A, 10 μL deionized water dropped on the deposited film using Syringe. A monochromatic light helps background to detect edges of droplet. Images of droplet captured by high resolution camera with pixel size of 1920 × 1080. Water contact angle was calculated using ImageJ software by applying drop analysis plugin.

Raman spectroscopy was performed with a Horiba LabRam HR spectrometer. Spectra were collected using Peltier-cooled CCD detector at 532 nm excitation and 100 X magnification objective with the confocal hole reduced to 100 μm to increase spatial resolution and hence ensure focus on the deposited films. The Raman laser used is a < 350 mW Cobalt Samba 100 and laser power at the sample surface was measured with a Thorlabs P100D power meter as 2.5 mW. The spectra were collected over the 60 – 1200 cm^{-1} range with spectral resolution of 1 cm^{-1}.

3. Results and discussion

3.1. TiO_2 and SiO_2 thickness calibration

Figures S1(a) and S1(b) display the transmission spectra for single-layer TiO_2 and SiO_2 films, respectively. The experimental data closely match the designed spectra, showing film thickness in control during deposition. The Swanepoel method [39] was employed to further validate TiO_2 film thickness and optical constants for three samples. Upper and lower envelope fitting shown in Figures (S2a–S2c), the estimated film thickness was approximately 268 nm, which was closely matching the design value of 270 nm (Fig. S3). The refractive index dispersion (Fig. S4) follows the Cauchy model, $n = A + B/\lambda^2 + C/\lambda^4$, with an average refractive index of ~2.41 at 500 nm, which was closer to the bulk value of 2.5 [40].

The porosity ratio of TiO_2 was calculated using the Eq. (4)

$$P = 1 - \left(n_p^{\,2} - 1\right)/\left(n_d^{\,2} - 1\right) * 100 \quad (4)$$

Where n_p, n_d, are the refractive index of deposited film containing nanoscale voids (porosity) and void free (bulk) films, respectively. The TiO_2 film showed a porosity of ~8 %, which is 51 % lower than that of films annealed at 300°C and prepared via RF magnetron sputtering [41]. For the SiO_2 film, Swanepoel analysis was not possible due to insufficient interference fringes. Nevertheless, the experimental spectrum (Fig. S1b) aligns well with the design, suggesting the film thickness closely approximates the target value of 275.6 nm.

3.2. Optical properties of multilayer AR coating

Fig. 1(a) shows the transmission spectrum of a single-side-coated sample deposited at 160°C. In the designed spectrum, the absorption region is located around 400 nm, whereas for the film deposited at 160°C, this region shifts to approximately 460 nm. This shift is attributed to slight variations in film thickness and refractive index between the designed and experimentally obtained values (see Fig. S3). However, the spectrum in the range of 460–1100 nm shows close agreement with the design, indicating that the discrepancies in this region are within an acceptable range. All spectra presented in the manuscript are plotted over the wavelength range of 400–1100 nm, as the focus of this study lies within this spectral region. The average transmission between 460 and 1100 nm was 94.82 ± 0.07 %, representing a 3.38 % increase compared to the uncoated substrate. Moreover, the optical transmission was increased by 4 ± 0.09 % at 532 nm and 3.38 ± 0.10 % at 1064 nm, respectively.

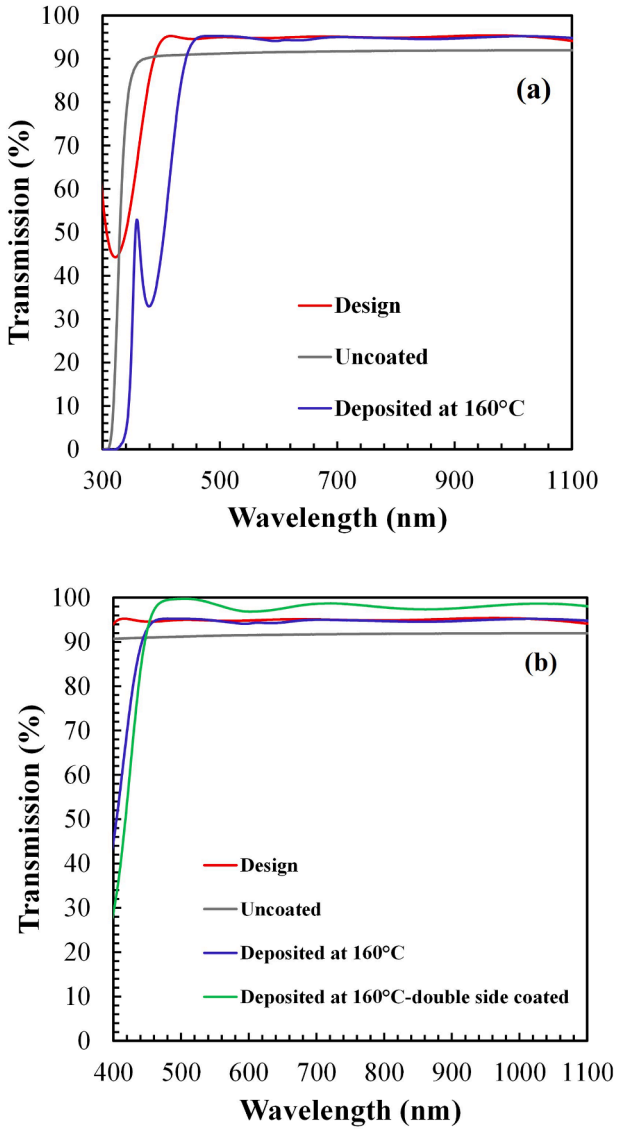

Fig. 1. Measured transmission spectra of SiO_2–TiO_2 AR coatings compared with the uncoated substrate. (a) Single-side deposition at a substrate temperature of 160°C. (b) Double-side deposition at the same substrate temperature.

Fig. 1(b) compares the optical transmission spectra of uncoated, single-side, and double-side coated samples. The double-side-coated sample deposited at 160°C achieved an average transmission of 98.14 ± 0.06 % over 460–1100 nm, representing a 6.54 % increase compared to the uncoated glass. Optical transmission at 532 nm and 1064 nm, increased up to 99.28 ± 0.10 % and 98.52 ± 0.09 %, respectively. This shows enhancements of 8.72 % and 7.13 % over the uncoated substrate. This enhancement is attributed to the increased level destructive interference from the double-side coated film due to alternating high (TiO_2)/ low (SiO_2) refractive index stack produces a phase shift that satisfies the condition for destructive interference of reflected waves at the air-film/ film-substrate/film-air interfaces and reduced total Fresnel reflections.

Fig. 2(a) show the reflectance spectra of uncoated, single-side coated, and double-side coated films in the wavelength range of 400–1100 nm. The single-side AR coating deposited at 160°C showed reflectance reduced by approximately 39.12 ± 0.02 % compared to the uncoated film over the range of 460–1100 nm. In contrast, the double-side coated AR film reduced average reflectance by 77.5 ± 0.07 %, which is almost twice the reduction achieved by the single-side AR coating. This manifests the double-side coated AR film showed significantly lower reflectance compared to the single-side coated AR film. The average reflectance of the double-side coated AR film was approximately 1.84 ± 0.02 % within the 460–1100 nm range, with the minimum average reflectance of just 0.26 % observed between 470 and 532 nm. Furthermore, at 532 nm and 1064 nm, the single-side coated AR film showed reflectance values of 4.5 ± 0.04 % and 4.89 ± 0.04 % representing reductions of 46.11 % and 38.56 % compared to the uncoated substrate. In comparison, the double-side coated AR film achieved reflectance values as low as 0.59 ± 0.06 % at 532 nm and 1.56 ± 0.04 % at 1064 nm, corresponding to reductions of 93.05 % and 80.40 %, respectively. The results show that the double-side coated AR film is significantly more effective in reducing reflection compared to the single-side coated AR film as shown in schematic diagram Fig. 2(b) and 2 (c).

Figures S5 (a–d) and S6 (a–d) show the transmission and reflectance spectra of films coated on both sides deposited at 120°C, 180°C, 200°C, and 240°C substrate temperature. All double-side coated AR films exhibited higher transmission and lower reflectance compared to the single-side coated AR film. To investigate effect of substrate temperature on transmission, the average transmission spectrum over the 460–1100 nm range was calculated and plotted as a function of substrate temperature in Fig. 3(a). The results show that increasing transmission trend with substrate temperature up to 180°C with highest average transmission of 98.23 ± 0.07 % is attributed to minimized scattering by a dense amorphous structure. However, as the substrate temperature increased to 240°C, the optical transmission decreased to 96.91 ± 0.09 %, which associated with formation of more porous structure, as discussed in Section 3.3. The maximum average transmission of 99.54 ± 0.04 % in the range 470 – 532 nm (Fig. 3(b)) and 98.63 ± 0.12 % in the range 950 – 1064 nm range (Fig. 3(c)) were achieved for films deposited at the substrate temperature of 160°C and 180°C, respectively.

Fig. 3(d) illustrates the transmission peak value at 532 nm and 1064 nm as a function of substrate temperature. At a substrate temperature of 120°C, the transmission increased by approximately 8.0 ± 0.05 % at 532 nm (indicated by solid white arrow mark) and 6.81 ± 0.10 % at 1064 nm (indicated by solid black arrow mark) compared to the uncoated substrate transmission at 532 nm and 1064 nm, respectively. This enhancement was further observed at 160°C, where transmission increased by 8.72 ± 0.10 % at 532 nm and 7.13 ± 0.08 % at 1064 nm. However, as the substrate temperature increased to 180°C, 200°C, and 240°C, the transmission improvement percentage reduced to 8.45 ± 0.08 %, 8.25 ± 0.07 %, 7.82 ± 0.02 % at 532 nm and 6.96 ± 0.11 %, 6.50 ± 0.06 %, 5.64 ± 0.03 % at 1064 nm. Transmission peak value in the range 460 – 1100, 470 – 532 nm, 950 – 1064 nm, 532 nm, 1064 nm, along with SME for each substrate temperature are shown in Table S1. The results indicate good reproducibility across all substrate temperatures, as evidenced by the low SME values. Based on these results, the optimized substrate temperature lies between 160°C and 180°C. The film deposited at 160°C exhibited highest transmission values of 99.28 ± 0.10 % at 532 nm and 98.52 ± 0.09 % at 1064 nm. Meanwhile, the film deposited at 180°C achieved maximum average transmission of 98.23 ± 0.07 % over the broad spectral range of 460 – 1100 nm. The average reflectance, calculated over the wavelength range of 460–1100 nm, is shown in Fig. 4. The lowest average reflectance of 1.71 ± 0.03 % was achieved at a substrate temperature of 180°C, whereas the reflectance increased to 2.56 ± 0.05 % when the substrate temperature was raised to 240°C. The decrease in transmission and the corresponding increase in reflectance are attributed to microstructural changes in the coating, as revealed by the AFM results.

3.3. Surface and microstructure analysis

Figs. 5 (a–e) present AFM images showing the microstructure of AR coatings deposited at various substrate temperatures. As shown in Fig. 5 (a), a smooth surface with nanoscale granular particles were observed from coating deposited at 120°C. At 160°C (Fig. 5(b)), the surface remains smooth, however grain coarsening and agglomeration was observed. The formation of these nanograins is attributed to the combined effect of plasma-induced crystallization and substrate temperature [42]. At 180°C, the film surface appears primarily smooth with fewer protruding particles (Fig. 5(c)), which is attributed to the formation of a dense amorphous structure with well-controlled morphology. However, as the substrate temperature increases the film surface turned to a rough texture with varying pore size (209.7 – 345 nm) at 200°C (Fig. 5(d)). The coating deposited at 240°C (Fig. 5(e)) exhibits a degraded microstructure characterized by numerous pores of varying sizes (182–463 nm), indicating increased structural disorder at elevated temperatures. In this framework, at moderate temperatures (160–180°C), ion bombardment and thermal activation act synergistically to promote dense, smooth, and optically optimal films. At higher temperatures (≥200°C), however, this balance shifts, leading to enhanced pore, and microstructural degradation despite continued ion assistance. The formation of these pores may be attributed to the trapping of Ar gas within the SiO_2 film during ion-assisted deposition. The trapped atoms can coalesce into aggregated nanobubbles, which subsequently release with higher substrate temperatures, leaving behind porous features in the film matrix. This phenomenon has also been reported in SiO_2 film prepared by IBS, where Ar entrapment and nanobubble evolution were observed upon thermal activation [43]. Nevertheless, a more detail experimental investigation such as cross-section scanning electron microscope (SEM) or transmission electron microscopy (TEM), gas desorption or mass spectroscopy analysis is required to confirm pore distribution and to elucidate the dominant mechanism governing pore formation at higher substrate temperatures.

Fig. 6(a) shows the average surface roughness (R_a) as a function of substrate temperature. A gradual increase in R_a is observed with increasing substrate temperature, reaching 305.95 ± 31.96 pm at 180°C, then stabilizing around 310 ± 37.3 pm at 200°C, and slightly decreasing to 309.6 ± 28.44 pm at 240°C. A similar trend is observed for the average RMS roughness (R_q), as shown in Fig. 6(b), where the R_q increases to 439.80 ± 80.74 pm at 180°C, saturates near 473.49 ± 69.92 pm at 200°C, and decreases to 418.47 ± 55.39 pm at 240°C. At 240°C, numerous nanoscale pores were formed, as seen in the Fig. 5(e), which modified the surface topography and redistributes the height variations, this led to a reduction in RMS roughness despite the presence of larger pores. Notably, the surface roughness values indicate that the surface remains exceptionally smooth, consistent with an amorphous structure. The pore size distribution was estimated using line profiles of the porous regions on the AFM image. Fig. 6(c) shows the average pore size as a function of substrate temperature. According to AFM results, pores begin to form after 180°C with average size of 289.8 ± 41.0 nm at 200°C. At 240°C, numerous pores were observed with an average size of

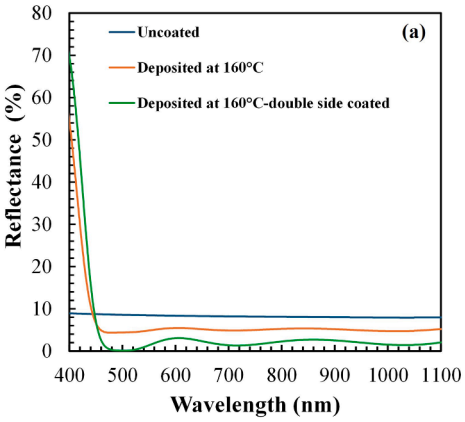

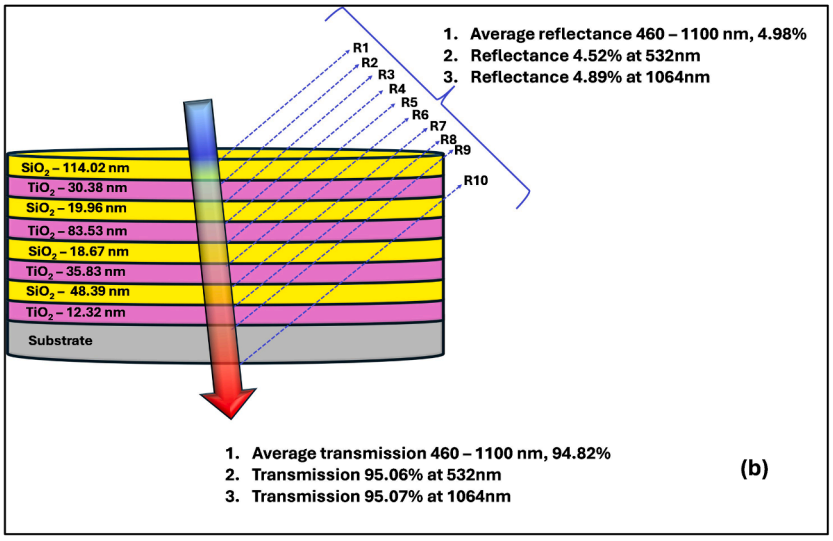

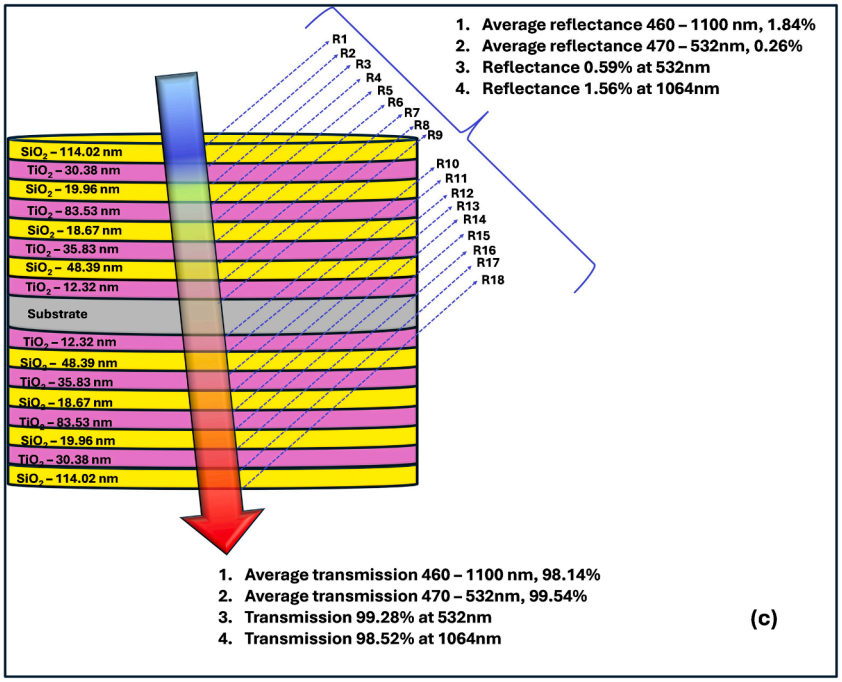

Fig. 2. (a) Comparison of measured reflectance spectra for single-side and double-side SiO_2–TiO_2 AR coatings deposited at a substrate temperature of 160°C. (b, c) Schematic diagrams illustrating the optical configuration of single-side and double-side AR coatings representing average transmission improvement and reflection loss in the broad wavelength range 460 – 1100 nm, 470 – 532 nm, 532 nm, and 1064 nm, respectively.

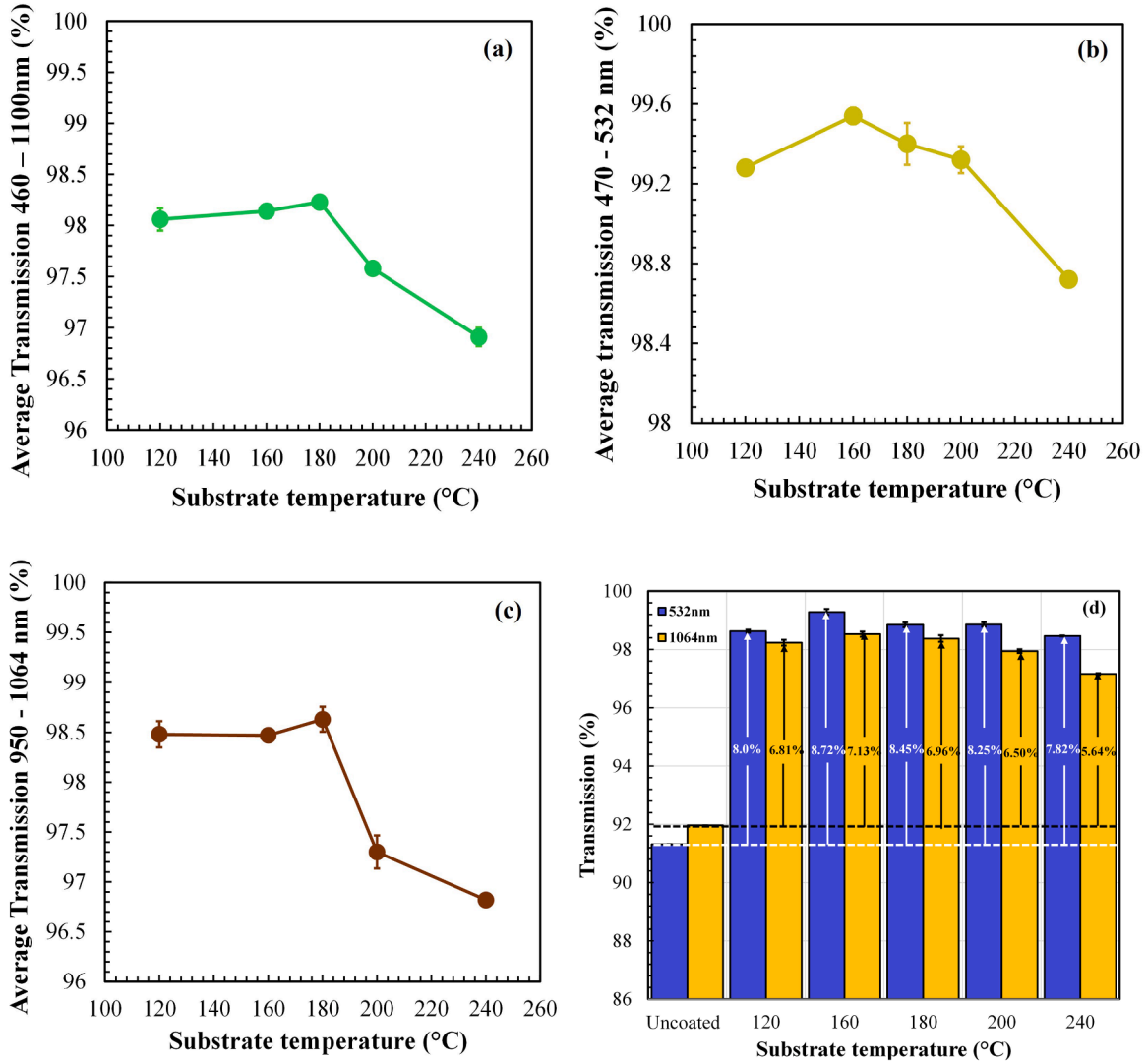

Fig. 3. Variation of optical transmission with substrate temperature: (a) average transmission in the 460–1100 nm range, (b) transmission in the 470–532 nm (visible) range, (c) transmission in the 950–1064 nm (NIR) range, and (d) percentage enhancement at 532 nm and 1064 nm relative to the uncoated substrate (indicated by white and black arrows).

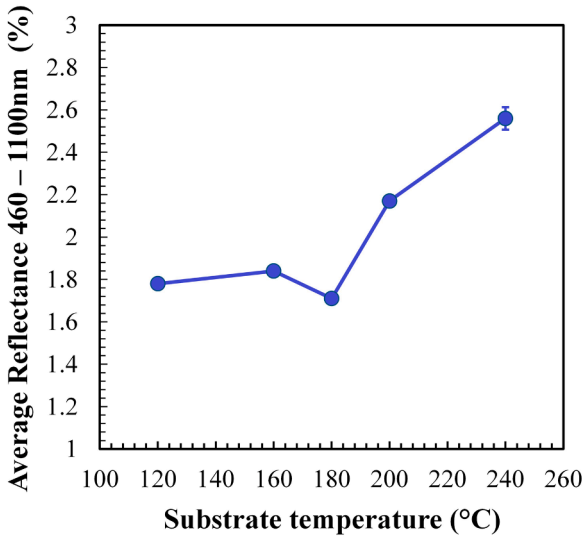

Fig. 4. Average reflectance of SiO_2–TiO_2 multilayer coatings, calculated over the 460–1100 nm range, as a function of substrate temperature.

300.54 ± 15.96 nm. The variation of grain size as function of substrate temperature is shown in Fig. 6(d). At 120°C, the average grain size was approximately 121.2 ± 19.12 nm, increasing to 313.2 ± 11.80 nm at 160°C, followed by a decrease at 180°C due to the dense packing of the amorphous structure. The grain size then remained nearly constant with further increases in substrate temperature, as pore formation became the dominant structural feature.

3.4. *Structural and phase analysis*

The presence of an amorphous phase with embedded nanocrystalline structures was confirmed by Raman spectroscopy. As shown in Fig. S7, all samples predominantly exhibited an amorphous structure, along with characteristic peaks of anatase TiO_2 at 144 cm^{-1}. Additionally, broad SiO_2 bands were observed at 458 cm^{-1}, 606 cm^{-1}, and 912 cm^{-1}. These Raman peaks are consistent with previously reported values [44, 45]. Notably, the detection of anatase TiO_2 indicates that the Raman laser was able to penetrate the top SiO_2 layer. The Raman signal intensity increased with substrate temperature up to 200°C, but decreased at 240°C, likely due to increased porosity. The broad SiO_2 peaks suggest a mixture of amorphous and nanocrystalline phases, which is in good agreement with the AFM results.

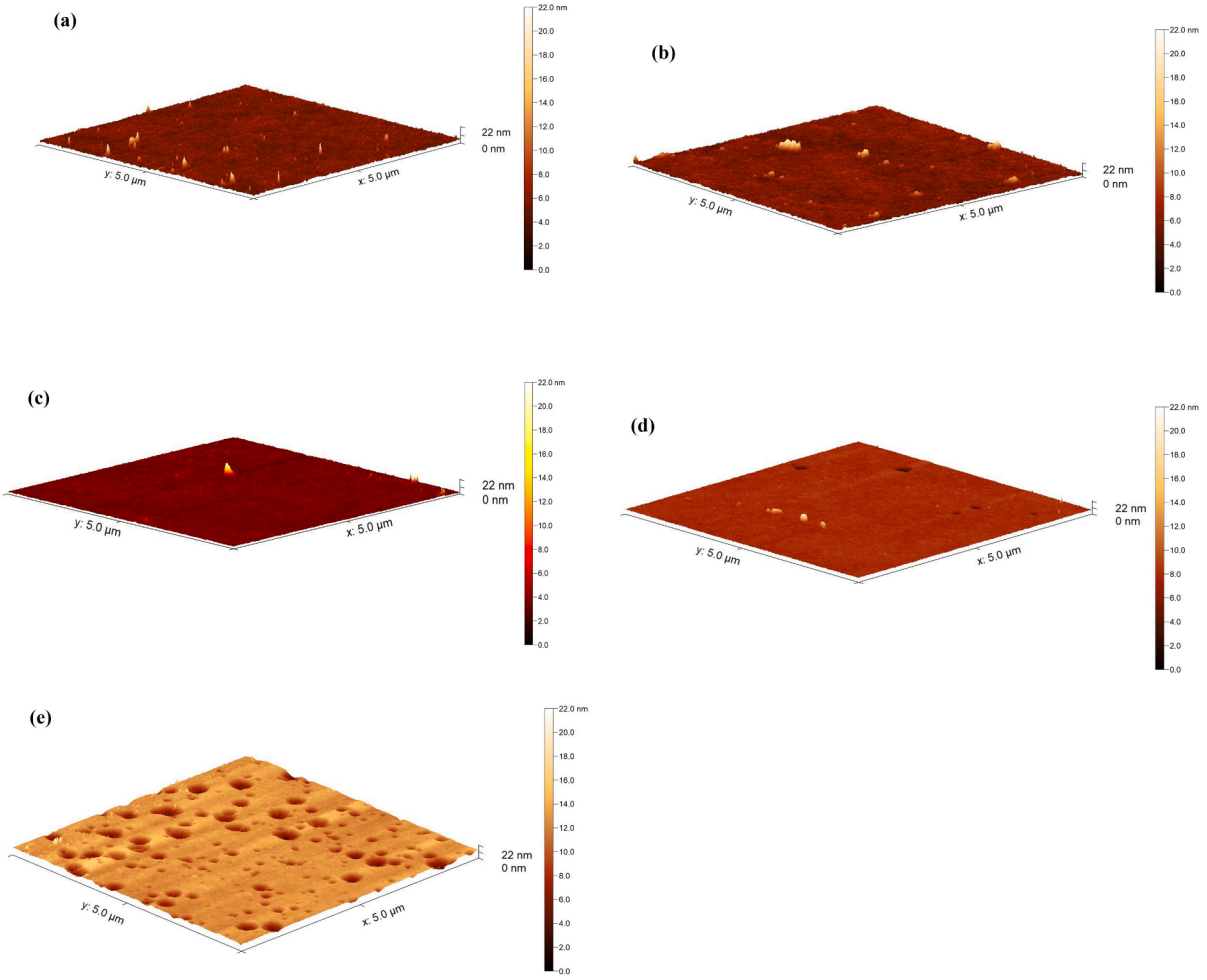

Fig. 5. AFM surface morphology images of SiO_2–TiO_2 AR coatings deposited at different substrate temperatures: (a) 120°C, (b) 160°C, (c) 180°C, (d) 200°C, and (e) 240°C.

3.5. Absorption coefficients

The presence of defects in the form of pores leads to surface absorption and optical scattering reducing the transmission of light through AR coating and supported by the Mie theory suggesting surface pores larger than 70 nm led to a significant reduction in transmission [46]. This validates the optical transmission reducing to 96.91± 0.09 % from AR coating deposited at 240°C in the 460–1100 nm range attributed to the distribution of variable pore size (182 – 463 nm) in the microstructure.

The absorption coefficient (α) was estimated using Eq. (5)

$$\alpha = 2.303 * A/d \quad (5)$$

Where α, A, and d is absorption coefficient, absorbance, and film thickness, respectively.

Fig. 7(a) shows the absorption coefficient of the double-side coated AR films as a function of wavelength. The AR film deposited at 180°C exhibited the lowest absorption coefficient, 0.288 ± 0.012 cm^{-1} at 603 nm and 0.232 ± 0.012 cm^{-1} at 847 nm. In contrast, higher absorption coefficients of 0.342 ± 0.006 cm^{-1} and 0.372 ± 0.06 cm^{-1} were observed for the film deposited at 200°C, as evidenced by a pronounced peak at 603 nm and 859 nm, respectively. At a substrate temperature of 240°C, the absorption coefficient increased further to 0.462 ± 0.012 cm^{-1} and 0.420 ± 0.012 cm^{-1}, with prominent peaks were observed at 608 nm and 900 nm. The increase in absorption coefficient at 200°C and 240°C is attributed to the defected microstructure of the film, characterized by the presence of pores. The average absorption coefficient over the range of 460–1100 nm is plotted as a function of substrate temperature in Fig. 7(b). The results show that the absorption coefficient decreases with increasing substrate temperature up to 180°C, reaching a minimum of 0.178 ± 0.012 cm^{-1}. However, at 240°C the absorption coefficient increased to 0.313 ± 0.012 cm^{-1} attributed to enhanced optical scattering.

3.6. Scattering factor

The effect of pore size on the scattering factor was calculated using Eq. (6):

$$S = \pi d/\lambda \quad (6)$$

Where S is the scattering factor, d is the average pore size, λ is the wavelength, and π is the constant, respectively. Fig. 8 shows the scattering factor of pores as a function of wavelength. The results indicated that large pore size, particularly for the film deposited at 240°C, lead to significantly higher scattering, especially at shorter wavelengths (e.g., 300 nm), where the pore size becomes comparable to the wavelength of incident light. As the wavelength increases, the scattering intensity decreases, which aligns well with prediction of Mie theory, where scattering is more pronounced when the pore size is comparable to the wavelength. This trend demonstrates that microstructural features such as pore size play a crucial role in determining the optical behaviour of AR coatings. The larger pores not only increase scattering losses but may also introduce irregularities in the refractive index distribution, which can further reduce optical performance. Therefore, controlling pore size

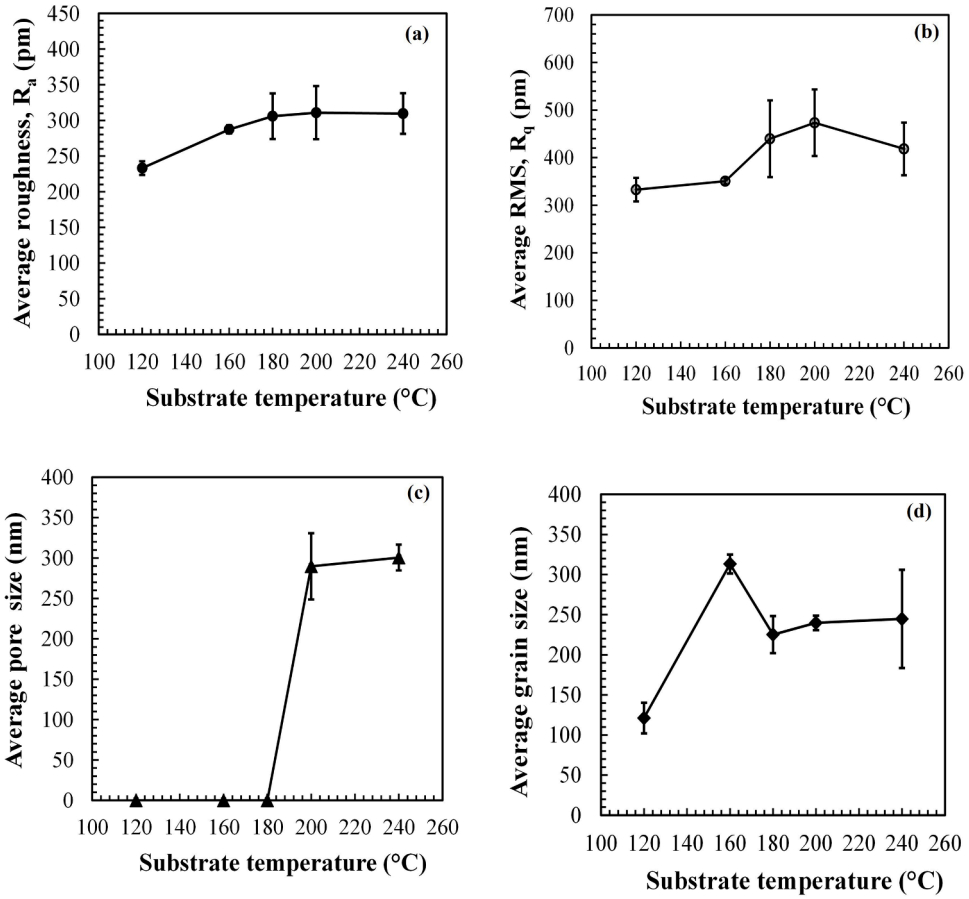

Fig. 6. Average surface parameters extracted from AFM data as a function of substrate temperature: (a) roughness (R_a), (b) RMS (R_q), (c) pore size, and (d) grain size.

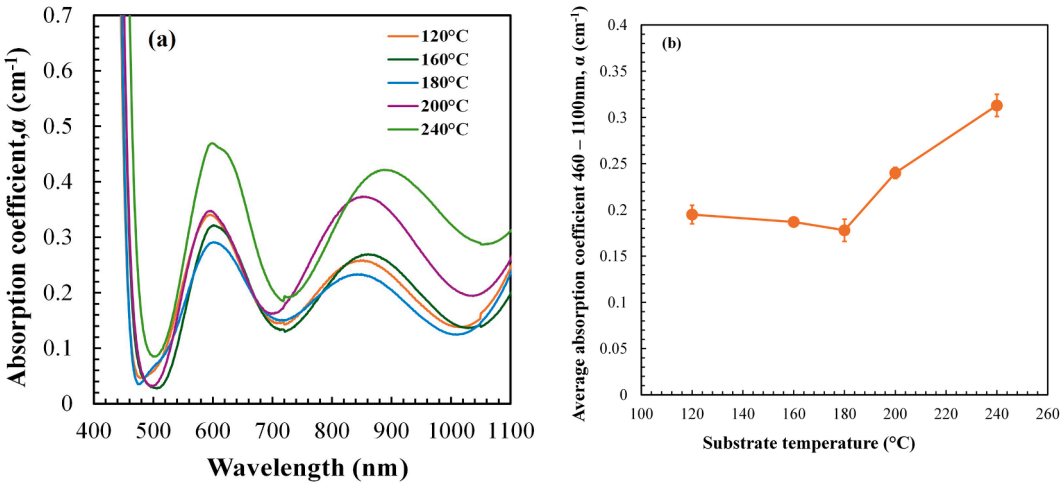

Fig. 7. (a) Spectral dependence of the absorption coefficient (α) for SiO_2–TiO_2 AR coatings.
(b) Average absorption coefficient (460–1100 nm) plotted versus substrate temperature.

during deposition is essential for optimizing the balance between film porosity and optical efficiency in SiO_2-TiO_2 multilayer AR coatings.

3.7. Adhesion test

Figures S8 (a–e) compare the optical transmission spectra of the SiO_2–TiO_2 films before and after the tape-peeling test. The transmission curves remain essentially unchanged for all samples deposited at different substrate temperatures, confirming that no optical degradation or delamination occurred following the adhesion test. This result demonstrates that the films maintain structural integrity and optical properties. In addition, adhesion strength was further evaluated using the cross-hatch tape test following the ASTM D3359 standard. The corresponding optical micrographs in Fig. 9 (a–e) show clean and intact cross-cut regions with no visible peeling, cracking, or edge lifting at any substrate temperature. According to the ASTM classification, all coatings achieved a Grade 5B rating, signifying excellent adhesion between the multilayer films and the substrate.

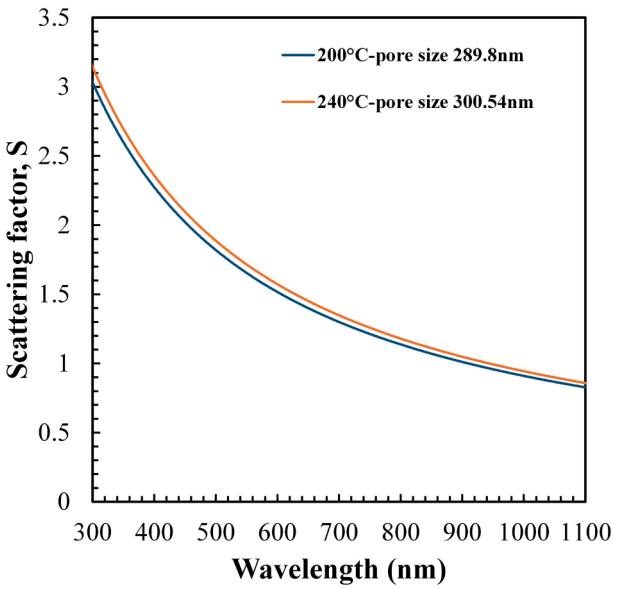

Fig. 8. Scattering factor of the films with pore size 289.8 ± 41.0 nm and 300.54 ± 15.96 nm as a function of wavelength.

The outstanding adhesion performance can be attributed to several interrelated factors intrinsic to the electron-beam ion-assisted deposition (EB-IAD) process. During deposition, energetic ion bombardment from the ion source enhances adatom mobility and stimulates interfacial intermixing between the initial SiO_2/TiO_2 layers and the substrate surface. This dynamic process produces a densified interfacial region with improved atomic packing. The substrate temperature also plays a key role in determining interfacial quality. At moderate temperatures (160°C and 180°C), enhanced surface diffusion allows atoms to arrange into stable bonding configurations without inducing thermal stress, leading to optimal adhesion. At higher temperatures (>200°C), although minor surface roughening and porosity appear, the adhesion remains robust due to the dense substructure established early in deposition.

3.8. Aging test

The optical transmission spectra before and after aging test are plotted as a function of wavelength in Fig. 10 (a–e). Results indicated insignificant change in transmission for all the AR coatings deposited except for 240°C. The stability of the lower-temperature coatings (< 200°C) can be explained by the compact amorphous microstructure achieved through ion-assisted deposition. The energetic ion bombardment during EB-IAD promotes densification, reduces surface porosity, and enhances interlayer adhesion, thereby limiting pathways for moisture penetration. The later exhibited a noticeable decrease transmission in Fig. 10(e) showing a reduction of approximately 0.66 % at 240°C. This decline is due to the microstructural coarsening and pore enlargement with average size of 300.54 ±15.96 nm occurs at elevated substrate temperature. Such large pores act as a scattering centre, and over time they can facilitate moisture absorption, modify the refractive index and increase diffusion scattering. These leads to decrease in the transmission after environmental exposure.

3.9. Water contact angle measurement

Figs. 11 (a–f) shows the images of water droplets on the AR coatings deposited at various substrate temperatures. The contact angle as a function of substrate temperature is shown in Fig. 11(g). Results show that the contact angle increases with increasing substrate temperature slightly up to 180°C as compared with uncoated substrate. The steep increment contact angle of 64.4° (± 1°) was observed at 240°C, which can be attributed to the increased porosity of the film and modified surface roughness. These pores trapped air beneath the droplet and reduced the effective solid-liquid contact area leading to increase the contact angle. Notably, film deposited at 160°C and 180°C contact angles were below 90°, confirming that the surfaces of films show hydrophilic behaviour, which can be suitable for self-cleaning purpose for solar cell thereby helping to maintain high optical transmission under real operating conditions.

4. Benchmarking against the state-of-the-art coating techniques

Compared to the state-of-the-art, the EB-IAD fabricated SiO_2–TiO_2 AR

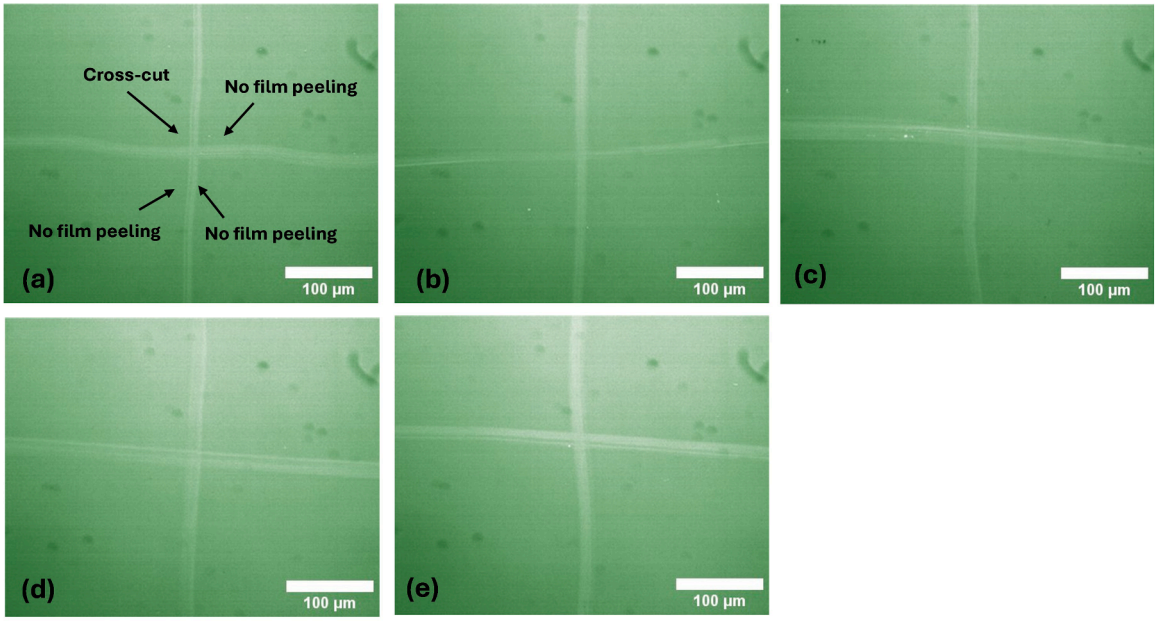

Fig. 9. Cross-hatch adhesion-test results for SiO_2–TiO_2 coatings deposited at substrate temperatures of (a) 120°C, (b) 160°C, (c) 180°C, (d) 200°C, and (e) 240°C. All coatings show Grade 5B according to ASTM D3359 standard, indicating strong adhesion with no film removal.

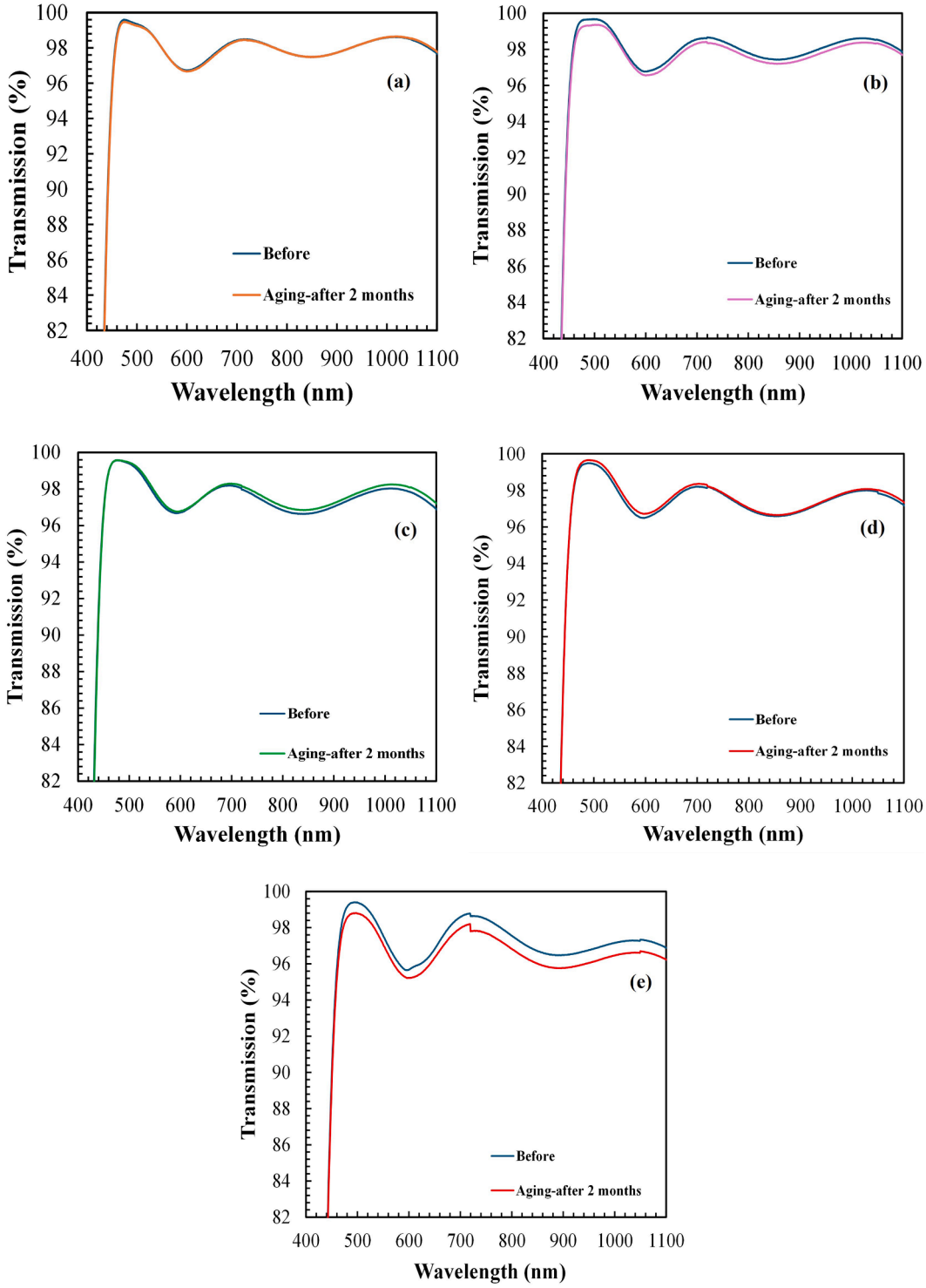

Fig. 10. Transmission spectra of SiO_2–TiO_2 AR coatings measured before and after two months of ambient aging for samples deposited at substrate temperatures of (a) 120°C, (b) 160°C, (c) 180°C, (d) 200°C, and (e) 240°C.

coatings presented in this work demonstrate competitive optical performance across major benchmarks. Advanced sol–gel multilayers have achieved high transmission, for example, Liu et al. reported a λ/4–λ/4 double-layer sol–gel design with an almost constant transmittance of 99.41 % across 450–900 nm with <1 % fluctuation, maintaining stability after two weeks at 50 % humidity [47], while Lin et al. achieved 98.8 % transmission at 550 nm [48]. Li et al. obtained 97.33 % transmission in the range 550 – 1100 nm using refractive index graded structure strategy by sol-gel [23]. Haritha et al. further improved durability by modifying the top SiO_2 layer with triethoxy(octyl)silane (OTES) treatment, maintaining 98.8 % transmission in the range 440 – 800 nm [49]. Despite these advances in optical performance, sol-gel coating often exhibits high porosity, weak adhesion, limited humidity resistance unless additional surface functionalization or post annealing is employed. IBS based multilayers achieved exceptionally low reflectance <0.001 % at the design line on large substrates [50] they often rely on porous layers or costly, high-complexity processing. Magnetron sputtered coating also provides dense, durable films with enhanced

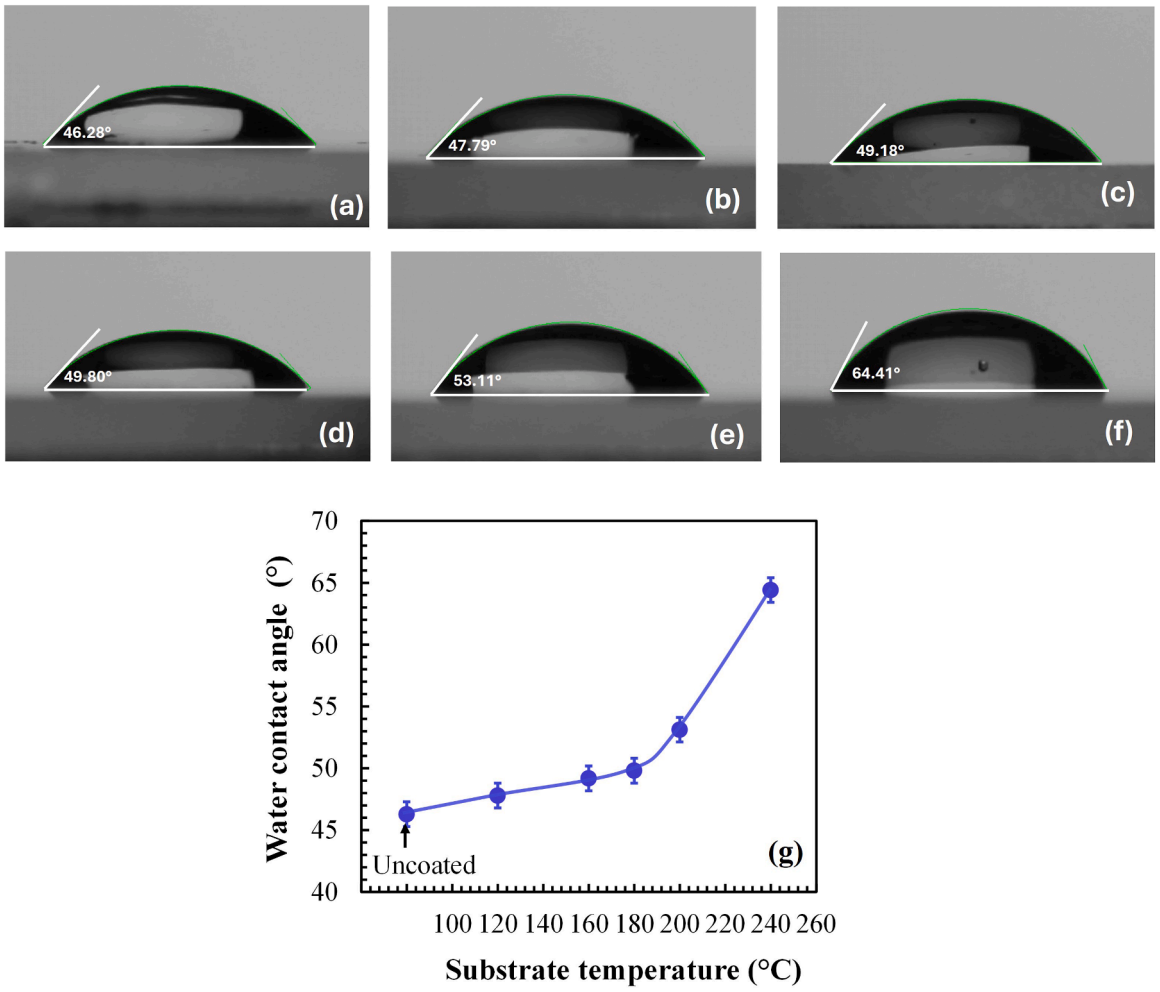

Fig. 11. Water contact angle images for (a) Uncoated substrate and SiO_2–TiO_2 AR coatings deposited at substrate temperatures of (b) 120°C, (c) 160°C, (d) 180°C, (e) 200°C, (f) 240°C, and (g) variation of water contact angle as a function of substrate temperature.

hardness, for example, Zambrano et al. improved hardness of AR coating about 7.0 GPa ± 0.7 GPa without degrading transmission 92.82 % in the range 400 – 700 nm by incorporating 1.at% Zr and thermal annealing at 400°C [26]. Mazur et al. reported exceeding transmission of 97 % in the range 460 – 800 nm and improved hardness of 9.34 GPa ± 0.3 GPa by adding a protective TiO_2 top layer using microwave assisted magnetron sputtering [6]. Jeong et al. reported up to 99.0 % transmission in the range 550 – 700 nm using RF magnetron [51], while Zhao et al. reported 93.19 % transmission in the broadband range 400 – 1000 nm using bilayer SiO_2/TiO_2 by magnetron sputtering [27]. EBD SiO_2-TiO_2 film reached average transmission of 90.02 % in the range 400 – 900 nm [32]. Previous EB-IAD studies achieved 95.21 % transmission in the range 400 - 640 nm by transforming amorphous TiO_2 through higher ion energy (750 eV) bombardment [52]. In contrast, the present study achieves transmittance of 99.54 % ± 0.04 in the 470–532 nm range and 98.63 ± 0.12 % in the range 950 −1064 nm, 99.28 ± 0.1 % at 532 nm and 98.52 ± 0.08 % at 1064 nm, together with a broadband average transmission of 98.23 ± 0.07 % over 460–1100 nm, using a relatively simple bilayer structure and moderate substrate temperature (160°C and 180°C) without post deposition annealing. Furthermore, film exhibited exceptionally low RMS_{avg} values (0.35 ± 0.006 nm at 160°C and 0.44 ± 0.08 nm at 180°C) and its strong adhesion led to reduced optical scattering. These results surpass most reported sol–gel and sputtering-based coating system under comparable spectral ranges as shown in the Table 2. This balances optical performance with processing practicality. Moreover, unlike porous sol–gel designs that often require additional hydrophobic treatments to ensure long-term stability [22].

To further highlight the advantage of EB-IAD over conventional EBD, a direct comparison was performed for SiO_2–TiO_2 coatings deposited at 160°C (Fig. S9). The EBD film exhibited an average transmission of 95.94 ± 0.10 % over 460–1100 nm, which is approximately 2.2 % lower than the corresponding EB-IAD AR coating (98.14 ± 0.06 %). In addition, absorption region in the EBD film was shifted to 514 nm. This behaviour is attributed to variations in film thickness, and refractive index. Although the EBD film showed slightly higher transmission at longer wavelengths (99.08 ± 0.07 % over 950–1064 nm and 99.70 ± 0.07 % at 1064 nm), a more detailed investigation is required to elucidate the origin of this long-wavelength enhancement. Overall, the dense microstructure achieved through EB-IAD coatings ensure inherent environmental durability and laser-grade adhesion without post-treatment. Therefore, the current approach stands out by offering broadband low reflectance, strong mechanical stability, and straightforward implementation in optical systems requiring moderate thermal budgets.

5. Conclusions

This study highlights the critical role of substrate temperature in optimizing the optical and structural performance of SiO_2–TiO_2 multilayer AR coating fabricated using EB-IAD process. Optimal transmission (up to 99.54 ± 0.04 %) and minimal reflectance (as low as 0.26 ± 0.02 %) were achieved at 160°C, with similarly excellent results were

Table 2
Comparison of optical transmission results for various substrate temperatures from published literature.

Preparation method	Material	Substrate temperature (°C)	Average transmission	Average transmission (%) 470 – 532nm	Average transmission (%) 950 – 1064nm	Transmission (%) at 532 nm	Transmission (%) at 1064 nm	Adhesion	Roughness	Reference
Sol-gel, dip coating	SiO_2-TiO_2/ SiO_2	Heat treated at 400°C for 2h	95.27 (400 – 1100 nm)	95.87	95.15	95.64	95.26	-	7 – 24.99 nm (R_a)	Ref [22]
Sol-gel, dip coating	SiO_2-TiO_2	Heat treated at 200°C for 30 min	97.33 (550 – 1100 nm)	-	95.74	-	95.66	-	-	Ref [23]
Sol-gel, dip coating	SiO_2-TiO_2	Heat treated at 400°C for 2h	99.41 (450 – 900 nm)	99.28		99.59		-	0.35 – 4.65 nm (R_q)	Ref [48]
Sol-gel, dip coating	SiO_2-TiO_2	Heat treated at 500°C for 2h	93.44 (400 – 1100 nm)	98.98	88.78	98.98	80.0	-	-	Ref [49]
Sol-gel, dip coating	SiO_2-TiO_2	Heat treated at 150°C for 1 h	98.8 (440 – 800 nm)	98.05		98.07		Excellent (Cross-hatch test)	-	Ref [50]
Magnetron sputtering	SiO_2-TiO_2	Room temperature	99.0 (550–700 nm)	98.80		98.96		-	1 – 10 nm (R_q)	Ref. [52]
Microwave assisted magnetron sputtering	SiO_2-TiO_2	< 100°C	97.41% (460 – 800 nm)	98.44		98.54		-	1. 5 nm (R_q)	Ref. [6]
RF magnetron sputtering	SiO_2-TiO_2	Room temperature	93.19 (400–1100 nm)	95.56	92.06	95.57	92.01	-	-	Ref. [27]
RF magnetron sputtering	Zr-doped (1.at %) SiO_2-TiO_2	Heat treated at 400°C for 1 h	92.82 (400 – 750 nm)	93.53		93.67		Good (observed by cross-section TEM)	0.96 – 1.96 nm (R_q)	Ref. [26]
E-beam evaporation	SiO_2-TiO_2	250°C	90.02 (400 – 900 nm)	88.94		89.79		-	-	Ref. [32]
E-beam evaporation	SiO_2-TiO_2	160°C	95.94 (460 – 1100 nm)	88.37	99.08	92.56	99.70	-	-	This work
EB + IAD	SiO_2-TiO_2	150°C	95.21 (400 – 640)	95.48		95.39		-	-	Ref. [53]
EB + IAD	SiO_2-TiO_2	160°C	98.14 (400–1100 nm)	99.54	98.47	99.28	98.52	Excellent (cross-hatch test)	0.35 ± 0.006 nm (R_q)	This work
EB + IAD	SiO_2-TiO_2	180°C	98.23 (400–1100 nm)	99.4	98.63	98.84	98.37	Excellent (cross-hatch test)	0.44 ± 0.08 nm (R_q)	This work

observed at 180°C. In contrast, substrate temperatures above 200°C led to microstructural degradation and reduced optical efficiency due to increased pores and micro-structural defects. The coating exhibited strong interfacial adhesion (ASTM 5B), environmental stability, and hydrophilic character. Overall, maintaining substrate temperatures *in-situ* between 160°C and 180°C yields high-performance broadband AR coating (460–1100 nm) suitable for manufacturing high damage threshold laser optics and high-efficiency solar energy applications.

CRediT authorship contribution statement

Omprakash Muthusamy: Writing – original draft, Investigation, Formal analysis, Data curation. **Yasir Joya:** Writing – review & editing, Supervision. **Richard Day:** Writing – review & editing, Supervision, Funding acquisition. **Chris Nyamayaro:** Writing – review & editing. **Ben Assinder:** Formal analysis. **Sohail Khan:** Formal analysis. **Matthew Jevon:** Investigation, Formal analysis. **Zengbo Wang:** Writing – review & editing, Supervision.

Declaration of competing interest

The authors declare that they have no known competing financial interests or personal relationships that could have appeared to influence the work reported in this paper.

Acknowledgements

This work was supported by the Ambition North Wales “Enterprise Engineering and Optics Centre” (EEOC) and the SMART Flexible Innovation Support (SFIS- 20240426).

Supplementary materials

Supplementary material associated with this article can be found, in the online version, at doi:10.1016/j.surfin.2026.109259.

Data availability

Data will be made available on request.

References

[1] G. San Vicente, R. Bayón, N. Germán, A. Morales, Long-term durability of sol–gel porous coatings for solar glass covers, Thin Solid Films 517 (2009) 3157–3160, https://doi.org/10.1016/j.tsf.2008.11.079.
[2] J. Szczyrbowski, G. Bräuer, G. Teschner, A. Zmelty, Large-scale antireflective coatings on glass produced by reactive magnetron sputtering, Surf. Coat. Technol. 98 (1998) 1460–1466, https://doi.org/10.1016/S0257-8972(97)00151-5.
[3] W. Dou, P. Wang, D. Zhang, J. Yu, An efficient way to prepare hydrophobic antireflective SiO_2 film by sol–gel method, Mater. Lett. 167 (2016) 69–72, https://doi.org/10.1016/j.matlet.2015.12.146.
[4] M.Keshavarz Hedayati, M. Elbahri, Antireflective coatings: conventional stacking layers and ultrathin plasmonic metasurfaces, a mini-review, Materials (Basel) 9 (2016) 497, https://doi.org/10.3390/ma9060497.
[5] T. Mizuta, T. Ikuta, T. Minemoto, H. Takakura, Y. Hamakawa, T. Numai, An optimum design of antireflection coating for spherical silicon solar cells, Sol. Energy Mater. Sol. Cells 90 (2006) 46–56, https://doi.org/10.1016/j.solmat.2005.01.010.
[6] M. Mazur, D. Wojcieszak, J. Domaradzki, D. Kaczmarek, S. Song, F. Placido, TiO_2/SiO_2 multilayer as an antireflective and protective coating deposited by microwave assisted magnetron sputtering, Opto-Electron. Rev. 21 (2013), https://doi.org/10.2478/s11772-013-0085-7.
[7] C. Yin, M. Zhu, T. Zeng, J. Sun, R. Zhang, J. Zhao, L. Wang, J. Shao, Al_2O_3 anti-reflection coatings with graded-refractive index profile for laser applications, Opt. Mater. Express 11 (2021) 875, https://doi.org/10.1364/OME.418174.
[8] M. Falmbigl, K. Godin, J. George, C. Mühlig, B. Rubin, Effect of annealing on properties and performance of HfO_2/SiO_2 optical coatings for UV-applications, Opt. Express 30 (2022) 12326, https://doi.org/10.1364/OE.453345.
[9] F. Chi, G. Wei, Q. Zhang, X. Sun, L. Zhang, X. Lu, L. Wang, F. Yi, X. Gao, Antireflective coatings with adjustable transmittance and high laser-induced damage threshold prepared by deposition of magnesium fluoride nanoparticles, Appl. Surf. Sci. 356 (2015) 593–598, https://doi.org/10.1016/j.apsusc.2015.07.183.
[10] S. LIEN, D. WUU, W. YEH, J. LIU, Tri-layer antireflection coatings (SiO_2/SiO_2–TiO_2/TiO_2) for silicon solar cells using a sol–gel technique, Sol. Energy Mater. Sol. Cells 90 (2006) 2710–2719, https://doi.org/10.1016/j.solmat.2006.04.001.
[11] L. Ye, Y. Zhang, X. Zhang, T. Hu, R. Ji, B. Ding, B. Jiang, Sol–gel preparation of SiO_2/TiO_2/SiO_2–TiO_2 broadband antireflective coating for solar cell cover glass, Sol. Energy Mater. Sol. Cells 111 (2013) 160–164, https://doi.org/10.1016/j.solmat.2012.12.037.
[12] M.M. Hasan, A.S.M.A. Haseeb, R. Saidur, H.H. Masjuki, M. Hamdi, Influence of substrate and annealing temperatures on optical properties of RF-sputtered TiO_2 thin films, Opt. Mater. (Amst) 32 (2010) 690–695, https://doi.org/10.1016/j.optmat.2009.07.011.
[13] N. Martin, C. Rousselot, D. Rondot, F. Palmino, R. Mercier, Microstructure modification of amorphous titanium oxide thin films during annealing treatment, Thin Solid Films 300 (1997) 113–121, https://doi.org/10.1016/S0040-6090(96)09510-7.
[14] M. Turowski, T. Amotchkina, H. Ehlers, M. Jupé, D. Ristau, Calculation of optical and electronic properties of modeled titanium dioxide films of different densities, Appl. Opt. 53 (2014) A159, https://doi.org/10.1364/AO.53.00A159.
[15] G. Bräuer, Large area glass coating, Surf. Coat. Technol. 112 (1999) 358–365, https://doi.org/10.1016/S0257-8972(98)00737-3.
[16] P.R. Sagdeo, D.D. Shinde, J.S. Misal, N.M. Kamble, R.B. Tokas, A. Biswas, A. K. Poswal, S. Thakur, D. Bhattacharyya, N.K. Sahoo, S.C. Sabharwal, Deposition and characterization of titania–silica optical multilayers by asymmetric bipolar pulsed dc sputtering of oxide targets, J. Phys. D. Appl. Phys. 43 (2010) 045302, https://doi.org/10.1088/0022-3727/43/4/045302.
[17] S. Kermadi, N. Agoudjil, S. Sali, L. Zougar, M. Boumaour, L. Broch, A.En Naciri, F. Placido, Microstructure and optical dispersion characterization of nanocomposite sol–gel TiO_2 –SiO_2 thin films with different compositions, Spectrochim. Acta A Mol. Biomol. Spectrosc. 145 (2015) 145–154, https://doi.org/10.1016/j.saa.2015.02.110.
[18] D. Wojcieszak, M. Mazur, D. Kaczmarek, J. Morgiel, G. Zatryb, J. Domaradzki, J. Misiewicz, Influence of Nd dopant amount on microstructure and photoluminescence of TiO_2:Nd thin films, Opt. Mater. (Amst) 48 (2015) 172–178, https://doi.org/10.1016/j.optmat.2015.07.040.
[19] E.L. Prociow, K. Sieradzka, J. Domaradzki, D. Kaczmarek, M. Mazur, Thin films based on nanocrystalline TiO_2 for Transparent Electronics, Acta Phys. Pol. A 116 (2009), https://doi.org/10.12693/APhysPolA.116.S-72. S-72-S-74.
[20] M. Mazur, J. Morgiel, D. Wojcieszak, D. Kaczmarek, M. Kalisz, Effect of Nd doping on structure and improvement of the properties of TiO_2 thin films, Surf. Coat. Technol. 270 (2015) 57–65, https://doi.org/10.1016/j.surfcoat.2015.03.019.
[21] D. Wojcieszak, M. Mazur, D. Kaczmarek, J. Morgiel, A. Poniedziałek, J. Domaradzki, A. Czeczot, Influence of the structural and surface properties on photocatalytic activity of TiO_2 :Nd thin films, Pol. J. Chem. Technol. 17 (2015) 103–111, https://doi.org/10.1515/pjct-2015-0037.
[22] X. Sun, K. Hu, J. Tu, K. Chen, Design and preparation of superhydrophobic, broadband and double-layer antireflective coatings, Surfaces and Interfaces 24 (2021) 101135, https://doi.org/10.1016/j.surfin.2021.101135.
[23] D. Li, D. Wan, X. Zhu, Y. Wang, Z. Han, S. Han, Y. Shan, F. Huang, Broadband antireflection TiO_2–SiO_2 stack coatings with refractive-index-grade structure and their applications to Cu(In,Ga)Se_2 solar cells, Sol. Energy Mater. Sol. Cells 130 (2014) 505–512, https://doi.org/10.1016/j.solmat.2014.07.042.
[24] C. Martinet, V. Paillard, A. Gagnaire, J. Joseph, Deposition of SiO_2 and TiO_2 thin films by plasma enhanced chemical vapor deposition for antireflection coating, J. Non. Cryst. Solids 216 (1997) 77–82, https://doi.org/10.1016/S0022-3093(97)00175-0.
[25] S.J. Lee, M.G. Hur, D.H. Yoon, Sol–Gel-derived nano-sized double layer anti-reflection coatings (SiO_2/TiO_2) for low-cost solar cell fabrication, J. Nanosci. Nanotechnol. 13 (2013) 7664–7668, https://doi.org/10.1166/jnn.2013.7845.
[26] D.F. Zambrano-Mera, R. Espinoza-González, R. Villarroel, A. Rosenkranz, N. Carvajal, M.I. Pintor-Monroy, A.G. Montaño-Figueroa, M.J. Arellano-Jiménez, M. Quevedo-López, P. Valenzuela, W. Gacitúa, Optical and mechanical properties of Zr-oxide doped TiO_2/SiO_2 anti-reflective coatings for PV glass covers, Sol. Energy Mater. Sol. Cells 243 (2022) 111784, https://doi.org/10.1016/j.solmat.2022.111784.
[27] L. Zhao, C. Zhao, L. Wang, X. Fan, Q. Wang, J. Liu, Preparation and optical properties of TiO_2/SiO_2 bilayer antireflection film, Opt. Mater. (Amst) 121 (2021) 111594, https://doi.org/10.1016/j.optmat.2021.111594.
[28] Q.-P. Lv, S.-W. Deng, S.-Q. Zhang, F.-Q. Gong, G. Li, Fabrication of broadband antireflection coatings using broadband optical monitoring mixed with time monitoring, Chin. Phys. B 26 (2017) 057801, https://doi.org/10.1088/1674-1056/26/5/057801.
[29] Q. Lv, M. Huang, S. Deng, G. Li, Fabrication of broadband antireflection coatings using wavelength-indirect broadband optical monitoring, Optik. (Stuttg) 156 (2018) 325–332, https://doi.org/10.1016/j.ijleo.2017.11.031.
[30] W.N. Zhang, J.L. Tu, A. Aierken, G.Y. Song, X.Z. Xu, P.Y. Yan, X.Y. Sun, K. Hu, L. Li, P.Q. Xu, Effect of 1 MeV electron irradiation on TiO_2/Al_2O_3/MgF_2 anti-reflective coating for GaInP/InGaAs/Ge triple junction solar cells, Opt. Mater. (Amst) 109 (2020) 110278, https://doi.org/10.1016/j.optmat.2020.110278.
[31] J.C.M. Model, A. Moehlecke, I. Zanesco, M. Ly, T.L. Marcondes, TiO_2 antireflection coating deposited by electro-beam evaporation: thin film thickness effect on weighted reflectance and surface passivation of silicon solar cells, Mater. Res. 25 (2022), https://doi.org/10.1590/1980-5373-mr-2022-0245.
[32] J.-S. Chen, S. Chao, J.-S. Kao, H. Niu, C.-H. Chen, Mixed films of TiO_2–SiO_2 deposited by double electron-beam coevaporation, Appl. Opt. 35 (1996) 90, https://doi.org/10.1364/AO.35.000090.

[33] R.X. Lim, M.S. Khor, K.Y. Cheong, Adhesion of electron-beam evaporated SiO_2/TiO_2 anti-reflective coating on ion-treated polycarbonate substrate under xenon arc accelerated weathering test, Mater. Chem. Phys. 315 (2024) 128960, https://doi.org/10.1016/j.matchemphys.2024.128960.
[34] S. Pongratz, A. Zöller, Plasma ion-assisted deposition: a promising technique for optical coatings, J. Vac. Sci. Technol. A: Vac., Surf., Films 10 (1992) 1897–1904, https://doi.org/10.1116/1.578112.
[35] J.R. McNeil, G.A. Al-Jumaily, K.C. Jungling, A.C. Barron, Properties of TiO_2 and SiO_2 thin films deposited using ion assisted deposition, Appl. Opt. 24 (1985) 486, https://doi.org/10.1364/AO.24.000486.
[36] C. Yang, H. Fan, Y. Xi, J. Chen, Z. Li, Effects of depositing temperatures on structure and optical properties of TiO_2 film deposited by ion beam assisted electron beam evaporation, Appl. Surf. Sci. 254 (2008) 2685–2689, https://doi.org/10.1016/j.apsusc.2007.10.006.
[37] A. Obstarczyk, U. Wawrzaszek, Influence of ion beam current on the structural, optical, and mechanical properties of TiO_2 coatings: ion beam-assisted vs conventional electron beam evaporation, Beilstein. J. Nanotechnol. 16 (2025) 1097–1112, https://doi.org/10.3762/bjnano.16.81.
[38] K.Narasimha Rao, S. Mohan, Influence of substrate temperature and post-deposition heat treatment on the optical properties of SiO_2 films, Thin Solid Films 170 (1989) 179–184, https://doi.org/10.1016/0040-6090(89)90722-0.
[39] N. Sahouane, A. Zerga, Optimization of antireflection multilayer for industrial crystalline silicon solar cells, Energy Procedia 44 (2014) 118–125, https://doi.org/10.1016/j.egypro.2013.12.017.
[40] S. Jena, R.B. Tokas, S. Thakur, D.V. Udupa, PRISA: a user-friendly software for determining refractive index, extinction co-efficient, dispersion energy, band gap, and thickness of semiconductor and dielectric thin films, Nano Express 2 (2021) 010008, https://doi.org/10.1088/2632-959X/abd967.
[41] Q. Ye, P.Y. Liu, Z.F. Tang, L. Zhai, Hydrophilic properties of nano-TiO_2 thin films deposited by RF magnetron sputtering, Vacuum 81 (2007) 627–631, https://doi.org/10.1016/j.vacuum.2006.09.001.
[42] M.M. Hasan, A.S.M.A. Haseeb, R. Saidur, H.H. Masjuki, M. Hamdi, Influence of substrate and annealing temperatures on optical properties of RF-sputtered TiO_2 thin films, Opt. Mater. (Amst) 32 (2010) 690–695, https://doi.org/10.1016/j.optmat.2009.07.011.
[43] C. Zhao, D. Child, D. Gibson, F. Placido, R.Y.Q. Fu, TiO_2 films prepared using plasma ion assisted deposition for photocatalytic application, Mater. Res. Bull. 60 (2014) 890–894, https://doi.org/10.1016/j.materresbull.2014.09.022.
[44] A. Paolone, E. Placidi, E. Stellino, M.G. Betti, E. Majorana, C. Mariani, A. Nucara, O. Palumbo, P. Postorino, M. Sbroscia, F. Trequattrini, M. Granata, D. Hofman, C. Michel, L. Pinard, A. Lemaitre, N. Shcheblanov, G. Cagnoli, F. Ricci, Argon and other defects in amorphous SiO_2 coatings for gravitational-wave detectors, Coatings 12 (2022) 1001, https://doi.org/10.3390/coatings12071001.
[45] S. Ben Khemis, E. Burov, H. Montigaud, D. Skrelic, E. Gouillart, L. Cormier, Structural analysis of sputtered amorphous silica thin films: a Raman spectroscopy investigation, Thin Solid Films 733 (2021) 138811, https://doi.org/10.1016/j.tsf.2021.138811.
[46] M. Lubas, J.J. Jasinski, M. Sitarz, L. Kurpaska, P. Podsiad, J. Jasinski, Raman spectroscopy of TiO_2 thin films formed by hybrid treatment for biomedical applications, Spectrochim. Acta a Mol. Biomol. Spectrosc. 133 (2014) 867–871, https://doi.org/10.1016/j.saa.2014.05.045.
[47] H. Shahbazi, M. Tataei, Influence of porosity on transparency behavior of $MgAl_2O_4$ spinel, experiment vs Mie theory, Opt. Mater. (Amst) 90 (2019) 289–299, https://doi.org/10.1016/j.optmat.2019.02.022.
[48] H. Liu, P. Wang, Q. Fan, J. Luo, P. Xiao, B. Jiang, $\lambda/4$–$\lambda/4$ double-layer broadband antireflective coatings with constant high transmittance, Coatings 12 (2022) 435, https://doi.org/10.3390/coatings12040435.
[49] W. Lin, J. Zheng, L. Yan, X. Zhang, Sol-gel preparation of self-cleaning SiO_2-TiO_2/SiO_2-TiO_2 double-layer antireflective coating for solar glass, Results Phys. 8 (2018) 532–536, https://doi.org/10.1016/j.rinp.2017.12.058.
[50] A.H. Haritha, K. Faturíková, A. Duran, D. Galusek, Y. Castro, J.J. Velázquez, High performance double layer hydrophobic antireflective coatings on glass prepared by sol–gel method, Open Ceramics 18 (2024) 100607, https://doi.org/10.1016/j.oceram.2024.100607.
[51] S. Dligatch, M. Gross, A. Chtanov, Ultra-low-reflectance, high-uniformity, multilayer-antireflection coatings on large substrates deposited using an ion-beam sputtering system with a customized planetary rotation stage, in: M. Lequime, H.A. Macleod, D. Ristau (Eds.), 2011: p. 816803. https://doi.org/10.1117/12.896747.
[52] S.-H. Jeong, J.-K. Kim, B.-S. Kim, S.-H. Shim, B.-T. Lee, Characterization of SiO_2 and TiO_2 films prepared using rf magnetron sputtering and their application to anti-reflection coating, Vacuum 76 (2004) 507–515, https://doi.org/10.1016/j.vacuum.2004.06.003.
[53] B. Fan, M. Suzuki, K. Tang, Ion-assisted deposition of TiO_2/SiO_2 multilayers for mass production, Appl. Opt. 45 (2006) 1461, https://doi.org/10.1364/AO.45.001461.